



In situ exsolution of silver nanoparticles on AgTaO₃-SrTiO₃ solid solutions as efficient plasmonic photocatalysts for water splitting

Jinxing Yu^{a,c,1}, Lei Zhang^{b,1}, Jun Qian^{b,**}, Zhirong Zhu^{c,***}, Shuang Ni^d, Gang Liu^{e,f}, Xiaoxiang Xu^{a,c,*}

^a Clinical and Central Lab, Putuo People's Hospital, Tongji University, 1291 Jiangning Road, Shanghai, 200060, China

^b Department of Neurosurgery, Tongji Hospital, Tongji University School of Medicine, 389 Xincun Road, Shanghai, 200065, China

^c Shanghai Key Lab of Chemical Assessment and Sustainability, School of Chemical Science and Engineering, Tongji University, 1239 Siping Road, Shanghai, 200092, China

^d Science and Technology on Plasma Physics Laboratory, Laser Fusion Research Center, China Academy of Engineering Physics, Mianyang, 621900, China

^e Shenyang National laboratory for Materials Science, Institute of Metal Research, Chinese Academy of Science, 72 Wenhua Road, Shenyang, 110016, China

^f School of Materials Science and Engineering, University of Science and Technology of China, 72 Wenhua Road, Shenyang, 110016, China

ARTICLE INFO

Keywords:

In situ exsolution
Plasmonic silver
Solid solution
Photocatalyst
Water splitting

ABSTRACT

Starting from two wide band gap semiconductors AgTaO₃ and SrTiO₃, we managed to reduce the band gap by forming their solid solutions, i.e. (AgTaO₃)_{1-x}(SrTiO₃)_x (0.0 ≤ x ≤ 1.0). These solid solutions all adopt cubic perovskite structure similar to SrTiO₃ and high temperature phase of AgTaO₃, suggesting that SrTiO₃ is helpful to stabilize AgTaO₃ in its high temperature cubic phase. Substantial improvements over photocatalytic hydrogen production were realized in these solid solutions which clearly outperform their parent compounds AgTaO₃ and SrTiO₃. *In-situ* exsolution of silver nanoparticles at the surface of solid solutions (x = 0.2) substantially strengthen the visible light absorption due to localized surface plasmons of these silver nanoparticles. This contributes to further improvements on both photocatalytic hydrogen and oxygen production under visible light illumination (λ ≥ 400 nm). Apparent quantum efficiency as high as ~ 2.02% and ~ 0.11% was achieved at solid solutions (x = 0.2) decorated with silver nanoparticles for full range (λ ≥ 250 nm) and visible light (λ ≥ 400 nm) illumination respectively. Photoelectrochemical analysis suggests that solid solutions own a better charge separation conditions than their parent compounds. Furthermore, the band edge positions of solid solutions (x = 0.2) lie approximately in the middle between AgTaO₃ and SrTiO₃, being ideal for solar water splitting reactions.

1. Introduction

The use of sunlight to split water into hydrogen and oxygen is a promising solution to cope with the energy crisis and environmental degradation [1]. This can be realized by semiconductor-based photocatalytic technology in which photons from solar irradiation is absorbed and is converted into chemical bonds in hydrogen [2–4]. Despite such an intriguing scenario, conventional semiconductors generally have wide band gaps, being inappropriate for solar photon harvesting [5]. For instance, about 43% of the total solar energy lies in visible light region and is transparent to these semiconductors. How to extend light absorption of conventional semiconductors is persistently an appealing topic [6].

It has been realized that doping serves as an effective means to improve the optical absorption of conventional semiconductors as it generally introduces additional bands/energy states inside the forbidden band gap of a semiconductor [7]. For instance, visible light absorption has been achieved for SrTiO₃ by various types of doping schemes such as Cr, Fe, Rh doping, La/Cr, La/N, La/N, Bi/Fe co-doping etc [8–17]. Nevertheless, doping refers to a relatively small incorporation of foreign atoms into the crystal structure therefore could be subject to side effects (defects formation) that are detrimental to photocatalytic activity [18,19]. In contrast, solid solution formation involves substantial substitution/dissolving one compound into another and has advantages in following aspects: (1) the crystal structures of these compounds will not be severely altered and can reduce defects

* Corresponding author at: Clinical and Central Lab, Putuo People's Hospital, Tongji University, 1291 Jiangning Road, Shanghai, 200060, China.

** Corresponding author.

*** Corresponding author.

E-mail addresses: qianjun19@126.com (J. Qian), zhuzhirong@tongji.edu.cn (Z. Zhu), xxxu@tongji.edu.cn (X. Xu).

¹ These authors contributed equally.

formation [15]; (2) light absorption or band gap values can be consecutively tuned [20]; (3) band edge positions can be tailored to meet thermodynamic requirements of a given reaction [21]. A wealth of solid solution photocatalysts have been prepared that often outperform their mother compounds such as $\text{Ga}_{1-x}\text{Zn}_x\text{N}_{1-x}\text{O}_x$ [2], $\text{AgGa}_{1-x}\text{In}_x\text{S}_2$ [22], and $(\text{AgIn})_x\text{Zn}_{2(1-x)}\text{S}_2$ [23], $\text{ZnGa}_{2-x}\text{Cr}_x\text{O}_4$ [24], etc. In particular, solid solutions with perovskite structures have gained considerable interest, not only because of many UV-active perovskite photocatalysts that are capable of direct water splitting but also due to the diversity of perovskite structures that is extremely tolerant to atom substitution/incorporation [25–28]. Previous investigations have witnessed a number of perovskite solid solutions that show appealing optical and photocatalytic properties such as $\text{La}_x\text{Sr}_{1-x}\text{TiO}_{3-x}\text{N}_x$ ($0 \leq x \leq 0.2$) [29], $\text{Bi}_x\text{Sr}_{1-x}\text{Ti}_{1-x}\text{Cr}_x\text{O}_3$ ($0 \leq x \leq 1$) [30], $\text{SrMg}_{x/3}\text{Nb}_{1-x/3}\text{O}_{2+y}\text{N}_{1-y}$ ($0 \leq x, y \leq 1$) [31], $\text{Sr}_{2-x}\text{La}_x\text{TiO}_{4-y}\text{N}_y$ ($0 \leq x \leq 0.5$) [32], $\text{BaCa}_{x/3}\text{Ta}_{1-x/3}\text{O}_{2+y}\text{N}_{1-y}$ ($0 \leq x, y \leq 1$) [33] etc. Band gap values and/or band edge positions can be easily tuned within these solid solutions and are responsible for the dramatic enhancements in their photocatalytic activities.

Perovskite AgTaO_3 and SrTiO_3 are well-known wide band gap photocatalysts demonstrating efficient activity for water splitting reactions under UV light irradiation [34–36]. The similar size of their constituent cations either at A or B sites suggest easy ion exchange and replacements during solid solution formation. More importantly, the large disparities in their band edge positions (AgTaO_3 : CBM ~ -1.0 V vs NHE, VBM ~ 2.5 V vs NHE; SrTiO_3 : CBM ~ -0.2 V vs NHE, VBM ~ 3.0 V vs NHE, pH = 0) implies a wide tunable window on the energetics of photo-generated charges if solid solutions between them can be formed. In this work, we have realized complete solubility between AgTaO_3 and SrTiO_3 , i.e. $(\text{AgTaO}_3)_{1-x}(\text{SrTiO}_3)_x$ ($0.0 \leq x \leq 1.0$). Their optical absorption, microstructures and photocatalytic activities were systematically explored. Strikingly, all solid solutions have smaller band gap values than their parent compounds AgTaO_3 ($E_g = 3.4$ eV) and SrTiO_3 ($E_g = 3.2$ eV). A minimal band gap of 2.97 eV was achieved at $(\text{AgTaO}_3)_{0.8}(\text{SrTiO}_3)_{0.2}$ ($x = 0.2$) which shows clear visible light absorption. This not only leads to enhancements on the UV light photocatalytic performance but also induces visible light photocatalytic activity. More interestingly, silver nanoparticles can be formed *in situ* at the surface of these solid solutions by a facile reduction method. These silver nanoparticles are plasmonically active under visible light illumination which further enhances the visible light absorption as well as photocatalytic activity.

2. Experimental

2.1. Materials synthesis

Solid solutions $(\text{AgTaO}_3)_{1-x}(\text{SrTiO}_3)_x$ ($0.0 \leq x \leq 1.0$) were prepared by standard polymerized-complex method: appropriate amounts of titanium butoxide (Aladdin, 99%), citric acid (Aladdin, 99.5%), tantalum chloride (Aladdin, 95%), strontium nitrate (SCR, 99.5%), and silver nitrate (SCR, 99.8%) were dissolved into ethylene glycol (Aladdin, GC grade). A few drops of deionized water were added to promote dissolution. The resultant transparent solution was magnetically stirred at 573 K for 3 h to facilitate polymerization. The brown resin obtained was then calcined at 823 K for 15 h to remove organic component. The resultant powders were ground using an agate mortar and pestle. The finely ground powders were then uniaxially pressed into pellets under a pressure of 5 MPa. The pellets were transferred into alumina crucibles and were calcined in a muffle furnace at 1173 K for 10 h. The calcined pellets were ground into powders again which were collected for further analysis.

Growth of silver nanoparticles on $(\text{AgTaO}_3)_{0.8}(\text{SrTiO}_3)_{0.2}$ ($x = 0.2$) was carried out according to our previous report [36]: 1 g of freshly prepared sample powders $(\text{AgTaO}_3)_{0.8}(\text{SrTiO}_3)_{0.2}$ ($x = 0.2$) were ultrasonically dispersed into 40 ml ethylene glycol to form a suspension. The suspension was magnetically stirring in a beaker which was heated to

433 K for reduction reactions. After 5 min, the beaker was transferred into ice water to terminate the reactions. The residual precipitant was centrifuged, washed with deionized water for three times and dried at 343 K for 24 h. The powders obtained were denoted as $\text{Ag}@x = 0.2$.

2.2. Materials analysis

Crystal structure and phase purity of freshly prepared sample powders were examined by X-ray powder diffraction (XRD) techniques on a Bruker D9 Focus diffractometer. Incident radiation was $\text{Cu K}\alpha_1$ ($\lambda = 1.5406 \text{ \AA}$) and $\text{Cu K}\alpha_2$ ($\lambda = 1.5444 \text{ \AA}$) and the step size for data collection was 0.01° with a collection time of 10 s for each step. Structure analysis and simulation on XRD data were performed by Rietveld refinement method embedded in the General Structure Analysis System (GSAS) software package [37]. A field emission scanning electron microscope (Hitachi S4800) and a transmission electron microscope (JEOL JEM-2100) were used to inspect microstructures of sample powders. Optical absorption spectra were collected in a diffuse reflectance mode on a UV-vis spectrophotometer (JASCO-V750) coupled with an integrating sphere. The reference non-absorbing material is BaSO_4 . Surface chemical compositions and binding energy of constitutional elements were analyzed using X-ray photoelectron spectroscopy (Thermo Escalab 250 with a monochromatic Al K α X-ray source). All binding energies were referenced to the adventitious carbon C 1s peak at 284.7 eV [38]. Surface areas were analyzed on a Micro-meritics instrument TriStar 3020 and were calculated via the Brunauer-Emmett-Teller (BET) model.

2.3. Photocatalytic hydrogen production

Photocatalytic experiments were carried out in a top-illumination-type reactor connected to a gas-closed circulation and evacuation system (Perfect Light, Lab solar-IIIAG). The temperature of the reactor was stabilized at about 293 K using water jacket with circulating water. In a typical experiment, 100 mg sample powders were dispersed into 100 ml aqueous solution containing either Na_2SO_3 (0.05 M) or silver nitrate (0.05 M). The former serves as a hole scavenger whilst the latter as an electron scavenger. The resultant suspensions were then sealed in the reactor and were evacuated for 60 min to remove air dissolved. Pt was photo-deposited onto sample powders as a co-catalyst to promote water reduction reactions according to previous reports [39,40]: appropriate amounts of H_2PtCl_6 aqueous solution were added into the suspensions which were then illuminated by a 500 W high-pressure mercury lamp (NBET, Merc-500) for 30 min. CoO_x , RuO_2 or Rh_2O_3 were loaded onto sample powders by a thermal decomposition method: proper amounts of $\text{Co}(\text{NO}_3)_3$ aqueous solution, RhCl_3 aqueous solution or ethyl acetone ruthenium THF solution was impregnated into sample powders to form slurry. The slurry was calcined at 673 K for 2 h to form CoO_x , Rh_2O_3 and RuO_2 . A 500 W high-pressure mercury lamp (NBET, Merc-500) was used as a light source. Visible light illumination was generated by filtering the output of the lamp with a UV cutoff filter ($\lambda \geq 400 \text{ nm}$). The photon flux of the lamp is calibrated using a quantum meter (Apogee MP-300). The recorded photon flux is $\sim 1543.9 \mu\text{mol m}^{-2} \text{ s}^{-1}$ for full range illumination ($\lambda \geq 250 \text{ nm}$) and $\sim 796.5 \mu\text{mol m}^{-2} \text{ s}^{-1}$ for visible light illumination ($\lambda \geq 400 \text{ nm}$). The Gas composition within the reactor was monitored using an online gas chromatograph (TECHCOMP, GC7900) (5 \AA molecular sieve columns and Ar carrier) coupled with a TCD detector. The apparent quantum efficiency (AQE) is then calculated using following equation:

$$\text{AQE} = \frac{2M_H}{M_p} \times 100\% \quad (1)$$

where M_H is the mole of hydrogen produced per hour and M_p is the mole of photon flux illuminated per hour.

2.4. Photoelectrochemical measurements

Sample powders were fabricated into photo-electrodes by an electrophoretic deposition method [41]: two pieces of clean fluorine doped tin oxide (FTO) glass (30×10 mm) were immersed into 50 mL acetone solution containing 40 mg sample powders and 10 mg iodine. A 10 mm distance was kept between the glasses which are in parallel with their conductive side facing inward. A potentiostatic control (Keithley 2450 Source Meter) was used to maintain a constant bias (15 V) between the glasses for 3 min. Sample depositions occurred at FTO glass on the anode side which was then used as the photo-electrodes. Calcination at 673 K for 60 min was applied to the freshly prepared photo-electrodes to remove residual iodine as well as to strengthen particle interconnection. The photo-electrodes were then immersed into diluted TiCl_4 (Alfa-Aesar, 99.9%) methanol solution (10 mM) and then dried in air. This operation was repeated for six times in order to minimize the exposure of naked FTO. The photo-electrodes were finally calcined at 673 K for 1 h under a protection of nitrogen flow (20 mL min^{-1}). The photoelectrochemical measurements were performed in a three-electrode configuration setup which was controlled by a Zahner electrochemical workstation. Photo-electrode, Pt foil (10×10 mm) and Ag/AgCl electrode were used as the working, counter and reference electrodes, respectively. An aqueous solution (15 ml) of $\text{K}_3\text{PO}_4/\text{K}_2\text{HPO}_4$ (0.1 M, pH = 7.95) was used as an electrolyte and a buffer. A 300 W Xenon lamp (Perfect Light, PLX-SXE300) coupled with a UV cutoff filter ($\lambda \geq 420 \text{ nm}$) was applied as the light source. The incident light was rectified by an electronic timer and shutter (DAHENG, GCI-73).

3. Results and discussion

3.1. Phase purity and crystal structure

The synthesis of AgTaO_3 or its solid solutions with other compounds is generally fraught with difficulties by conventional solid state reactions [42]. This is largely due to the thermal instability of Ag^+ at elevated temperatures under which solid state reactions are performed [43]. In this work, we adopted standard polymerized-complex method to synthesize AgTaO_3 and its solid solutions with SrTiO_3 . This wet method significantly reduces reaction temperature to a point (1173 K) that stays away from the thermal instability region of AgTaO_3 ($> 1373 \text{ K}$), thereby favoring single phase formation. X-ray powder diffraction (XRD) patterns of all samples, namely, $(\text{AgTaO}_3)_{1-x}(\text{SrTiO}_3)_x$ ($0.0 \leq x \leq 1.0$) are illustrated in Fig. 1a. Previous studies using *in-situ* Synchrotron X-ray powder diffraction techniques suggest that AgTaO_3 adopts a cubic structure ($Pm\bar{3}m$) at high temperatures ($> 853 \text{ K}$) which undergoes sequential phase transformations to tetragonal ($P4/mbm$), orthorhombic ($Cmcm$) and rhombohedral ($R3c$) one [44]. The stable rhombohedral structure ($R3c$) at room temperature stems from cation

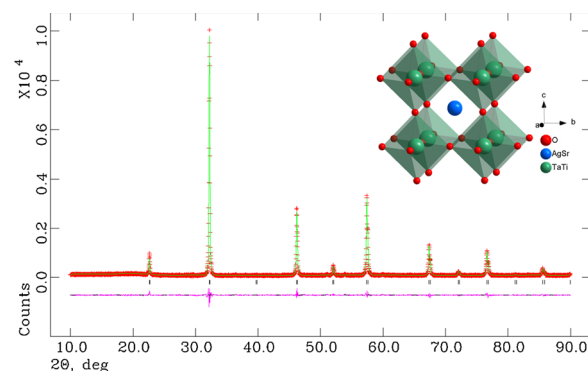


Fig. 2. Observed and calculated X-ray powder diffraction patterns of $(\text{AgTaO}_3)_{0.8}(\text{SrTiO}_3)_{0.2}$ ($x = 0.2$); the refinement using the $Pm\bar{3}m$ space group converges with good R factors and χ^2 factor ($R_p = 7.40\%$, $R_{wp} = 6.24\%$, $\chi^2 = 1.704$). Schematic illustration of refined crystal structure is displayed as an inserted image.

displacements along $[111]_p$ direction which couples with antiphase tilts ($a^-a^-a^-$ in Glazer notation) of TaO_6 octahedrons, resulting in a $\sqrt{2}a_p \times \sqrt{2}a_p \times \sqrt{12}a_p$ superstructure compared to prototype cubic cell a_p . [44] This is rationalized by the split X-ray reflections of AgTaO_3 around 32° if compared with cubic SrTiO_3 (Fig. 1a). Very interestingly, introducing merely 20% SrTiO_3 into the structure of AgTaO_3 transforms the rhombohedral structure to the cubic one, as evidenced by the degenerate reflection at 32° . Therefore, formation of AgTaO_3 - SrTiO_3 solid solutions helps to stabilize AgTaO_3 in the cubic structure. Complete solid solutions between AgTaO_3 and SrTiO_3 have been achieved with slight shift of all reflections towards high angles, indicating gradual shrinkage of cubic unit cell. This is reasonable as Sr^{2+} and Ti^{4+} are smaller than Ag^+ and Ta^{5+} , respectively [45]. In addition, reducing $(\text{AgTaO}_3)_{0.8}(\text{SrTiO}_3)_{0.2}$ ($x = 0.2$) by ethylene glycol at 433 K has little impact to its XRD patterns (Fig. 1b), suggesting that crystal integrity is maintained under reduction reactions. We then performed Rietveld refinement on all XRD data obtained. A typical refined XRD patterns for $(\text{AgTaO}_3)_{0.8}(\text{SrTiO}_3)_{0.2}$ ($x = 0.2$) is illustrated in Fig. 2. Reasonable goodness-of-fit parameters were achieved only assuming that Ag and Sr, Ti and Ta occupy the same crystallographic positions, respectively. The substitution between Ag and Sr, Ti and Ta is most likely random as neither super-lattice reflections nor reflection splits are observed. The refined unit cell parameters are tabulated in Table 1. Decrease of unit cell parameters can be seen by increasing the level of SrTiO_3 in the structure, being consistent with previous expectations.

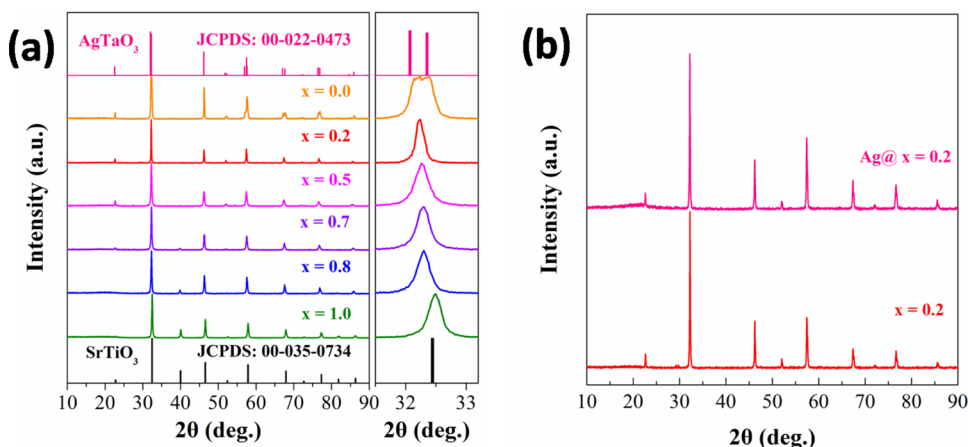


Fig. 1. (a) X-ray powder diffraction (XRD) patterns of solid solutions $(\text{AgTaO}_3)_{1-x}(\text{SrTiO}_3)_x$ ($0.0 \leq x \leq 1.0$), standard patterns of AgTaO_3 (JCPDS: 00-022-0473) and SrTiO_3 (JCPDS: 00-035-0734) are also included for comparisons, enlargement of the most intensive reflection is shown on the right side; (b) XRD patterns of $(\text{AgTaO}_3)_{0.8}(\text{SrTiO}_3)_{0.2}$ ($x = 0.2$) before and after reduction reactions.

Table 1

Space group, unit cell parameters, BET surface area and band gap values of solid solutions $(\text{AgTaO}_3)_{1-x}(\text{SrTiO}_3)_x$ ($0.0 \leq x \leq 1.0$). Sample $(\text{AgTaO}_3)_{0.8}(\text{SrTiO}_3)_{0.2}$ ($x = 0.2$) after reduction reactions was also included for comparisons, standard deviation is included in the parenthesis.

| Sample | Space group | $a / \text{\AA}$ | $c / \text{\AA}$ | $V / \text{\AA}^3$ | BET surface area (m^2/g) | Band gap (eV) |
|---------------------|--------------|------------------|------------------|--------------------|--|---------------|
| $x = 1.0$ | $Pm\bar{3}m$ | 3.9065(2) | – | 59.618(5) | 5.0(1) | 3.26(1) |
| $x = 0.8$ | $Pm\bar{3}m$ | 3.9189(1) | – | 60.188(4) | 4.7(1) | 3.20(1) |
| $x = 0.7$ | $Pm\bar{3}m$ | 3.9256(2) | – | 60.494(5) | 4.5(1) | 3.15(1) |
| $x = 0.5$ | $Pm\bar{3}m$ | 3.9362(2) | – | 60.987(7) | 4.4(1) | 3.07(1) |
| $x = 0.2$ | $Pm\bar{3}m$ | 3.9305(1) | – | 60.722(3) | 1.9(1) | 2.97(1) |
| $\text{Ag}@x = 0.2$ | $Pm\bar{3}m$ | 3.9304(1) | – | 60.716(3) | 1.8(1) | 2.84(1) |
| $x = 0.0$ | $R\bar{3}c$ | 5.5320(2) | 13.6867(6) | 362.75(3) | 1.8(1) | 3.41(1) |

3.2. Microstructures

The microstructures of as-prepared solid solutions $(\text{AgTaO}_3)_{1-x}(\text{SrTiO}_3)_x$ ($0.0 \leq x \leq 1.0$) were then inspected under electron microscopy conditions. Fig. 3 displays typical field emission scanning electron microscopy images of all sample powders. These sample powders are composed of irregular particles whose particle size is strongly correlated with SrTiO_3 content in the solid solutions. For instance, pristine SrTiO_3 ($x = 1.0$) contains small granules with the size less than 100 nm (Fig. 3a) whilst the particle size is monotonically increased to more than 500 nm when the level of SrTiO_3 in the solid solutions decreased to $x = 0.2$. Nevertheless, particle size is decreased back slightly when SrTiO_3 content is further reduced to $x = 0.0$, i.e. pristine AgTaO_3 . It has to be mentioned that all particles have a clean and smooth surface, suggesting phase segregations, such as exsolution of metallic Ag is not observed [35]. EDS mapping also suggests that all constituent elements are homogeneously distributed (Figure S1). This can be attributed to the wet synthetic method that avoids high temperature calcination processes. However, tiny grain-like particles less than 50 nm appear when sample $(\text{AgTaO}_3)_{0.8}(\text{SrTiO}_3)_{0.2}$ ($x = 0.2$) is treated in the hot ethylene glycol. This is further confirmed by transmission electron microscopic image (TEM) where small granules of ~ 20 nm emerge at the surface of bulky particles. These tiny granules, according to our previous study, belong to metallic silver due to reduction and exsolution of lattice Ag in the perovskite structures. The size of these metallic Ag falls into the region that shows localized surface plasmons under visible light illumination, therefore, turns the color of sample powders from yellowish white to yellow (see digital photo in Fig. 3h). EDS analysis of sample $\text{Ag}@x = 0.2$ before and after nitric acid (2 M) treatment suggest that about 4 mol% Ag is reduced and exsolved

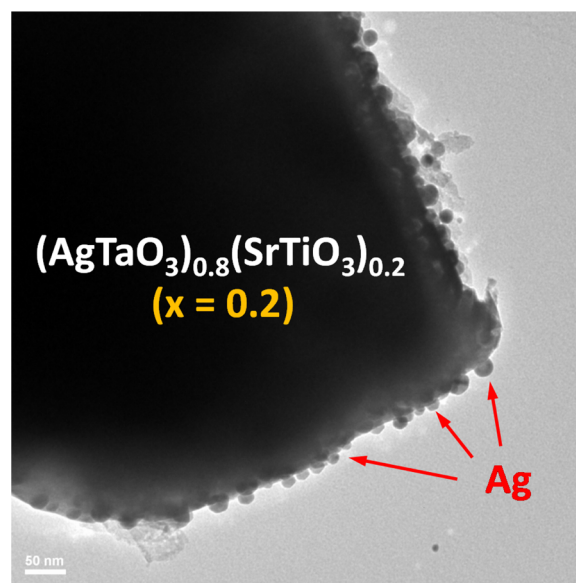


Fig. 4. Transmission electron microscopy image of $(\text{AgTaO}_3)_{0.8}(\text{SrTiO}_3)_{0.2}$ ($x = 0.2$) after reduction reactions, silver nanoparticles can be easily identified at the edge of individual bulky particles.

(Fig. 4).

The UV-vis absorption of solid solutions shows interesting features that differs largely from their parent compounds AgTaO_3 and SrTiO_3 . Pristine AgTaO_3 and SrTiO_3 are typical wide band gap semiconductors that own absorption edge in the UV light region ($\lambda < 400 \text{ nm}$) (Fig. 5a). However, the absorption edge of solid solutions $(\text{AgTaO}_3)_{1-x}(\text{SrTiO}_3)_x$ ($0.0 < x < 1.0$) is clearly red shifted into visible light region. In particular, $(\text{AgTaO}_3)_{0.8}(\text{SrTiO}_3)_{0.2}$ ($x = 0.2$) displays an absorption edge as far as 430 nm, being active to visible light photons. The band gap values of all samples were then determined by Kubelka-Munk transformation and extrapolating the linear part down to energy axis. The data are summarized in Table 1. It is clear from Table 1 that band gap is narrowed after combining AgTaO_3 and SrTiO_3 into solid solutions, which shows a minimal value of 2.97 eV at $x = 0.2$. More interestingly, the absorption edge is further red-shifted when exsolving metallic Ag at the surface of sample $(\text{AgTaO}_3)_{0.8}(\text{SrTiO}_3)_{0.2}$ ($x = 0.2$) (see Fig. 5c). This can be rationalized by the strong plasmonic absorption of metallic Ag around 450 nm, contributing to a nominal band gap of 2.8 eV. The anchorage of metallic Ag nanoparticles at the surface of $(\text{AgTaO}_3)_{0.8}(\text{SrTiO}_3)_{0.2}$ ($x = 0.2$) shall be highly beneficial for photocatalysis as localized surface plasmons can inject hot electrons to the substrate and/or boost electron-hole pair generation.

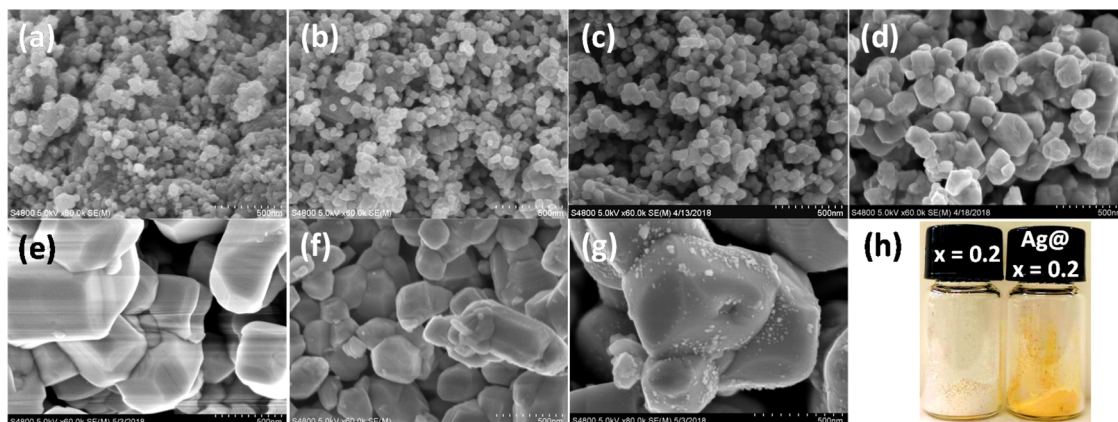


Fig. 3. Field emission scanning electron microscopy images of solid solutions $(\text{AgTaO}_3)_{1-x}(\text{SrTiO}_3)_x$ ($0.0 \leq x \leq 1.0$): (a) $x = 1.0$, (b) $x = 0.8$, (c) $x = 0.7$, (d) $x = 0.5$, (e) $x = 0.2$, (f) $x = 0.0$, (g) $x = 0.2$ after reduction reactions, (h) digital photograph of $x = 0.2$ before and after reduction reactions, respectively.

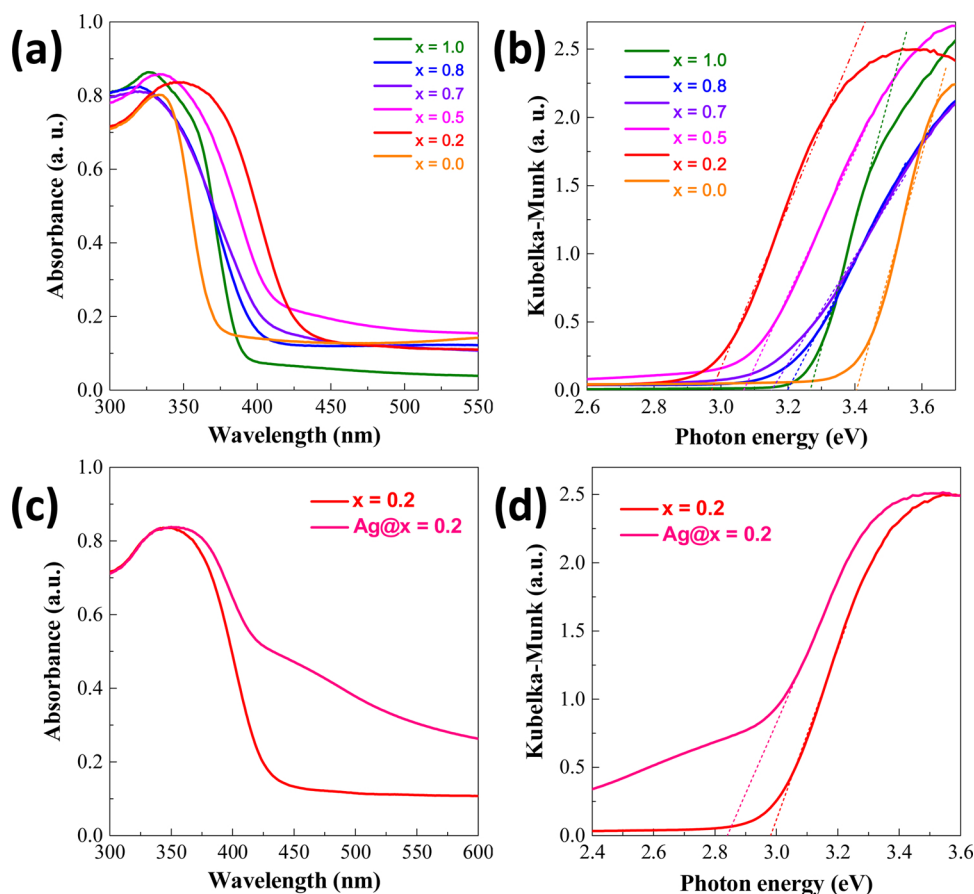


Fig. 5. (a) UV-vis light absorption spectra (converted from diffuse reflectance spectra) of solid solutions $(\text{AgTaO}_3)_{1-x}(\text{SrTiO}_3)_x$ ($0.0 \leq x \leq 1.0$), (b) Kubelka-Munk transformation of diffuse reflectance data of (a); (c) UV-vis light absorption spectra of $(\text{AgTaO}_3)_{0.8}(\text{SrTiO}_3)_{0.2}$ ($x = 0.2$) before and after reduction reactions; (d) Kubelka-Munk transformation of diffuse reflectance data of (c).

3.3. X-ray photoelectron spectroscopy

The surface conditions for solid solutions and their parent compounds are examined by X-ray photoelectron spectroscopy (XPS). Spectra of core-level electrons for Ag 3d and O 1s are illustrated in Fig. 6. Overlapping peaks is unfolded by fitting with different Gaussian-Lorentzian functions and all data point has been adjusted by referencing to the adventitious C 1s peak at 284.7 eV. For Ag 3d state, two peaks due to spin-orbital splitting can be identified for pristine AgTaO_3 which are centered around 373.6 eV and 367.6 eV for $3d_{3/2}$ and $3d_{5/2}$ state, respectively. These two peaks are shifted slightly to a higher binding energy for solid solutions ($x = 0.2$). This might be explained by a change of crystal structure from rhombohedral symmetry to cubic one

that increases the ionic bond strength between Ag and O. Reduction of solid solutions ($x = 0.2$) with hot ethylene glycol leads to two strong peaks at 373.0 eV and 367.0 eV, corresponding to metallic Ag [36]. These results are consistent with previous observations in SEM, TEM and UV-vis absorption spectra that Ag nanoparticles exsolute out from sample particles. For O 1s state, two overlapping peaks centered around 529 eV and 531 eV can be identified. These two peaks are frequently seen in a number of metal oxide compounds and are ascribed to lattice oxygen (O^{2-}) and surface hydroxyl groups (OH^-) [46]. The latter one seems to be enhanced in solid solutions ($x = 0.2$), particularly after reduction in hot ethylene glycol ($\text{Ag}@x = 0.2$).

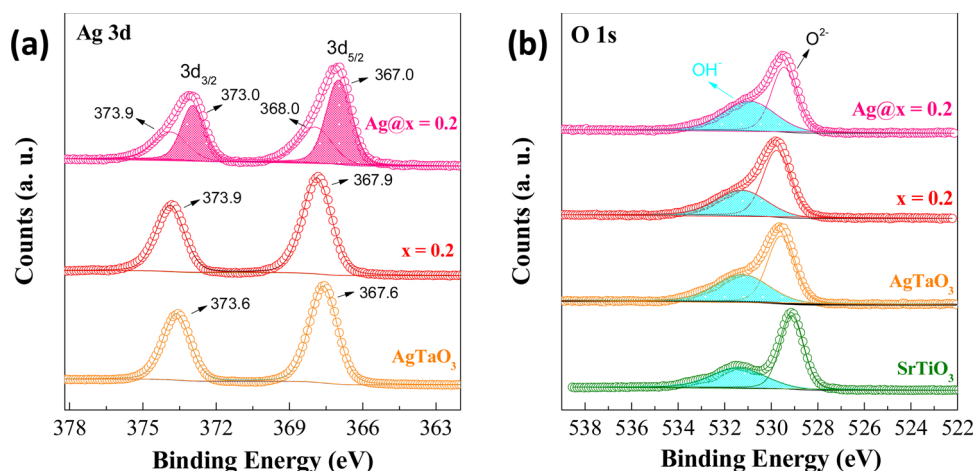


Fig. 6. XPS spectra of freshly prepared sample powders: (a) Ag 3d state, (b) O 1s state.

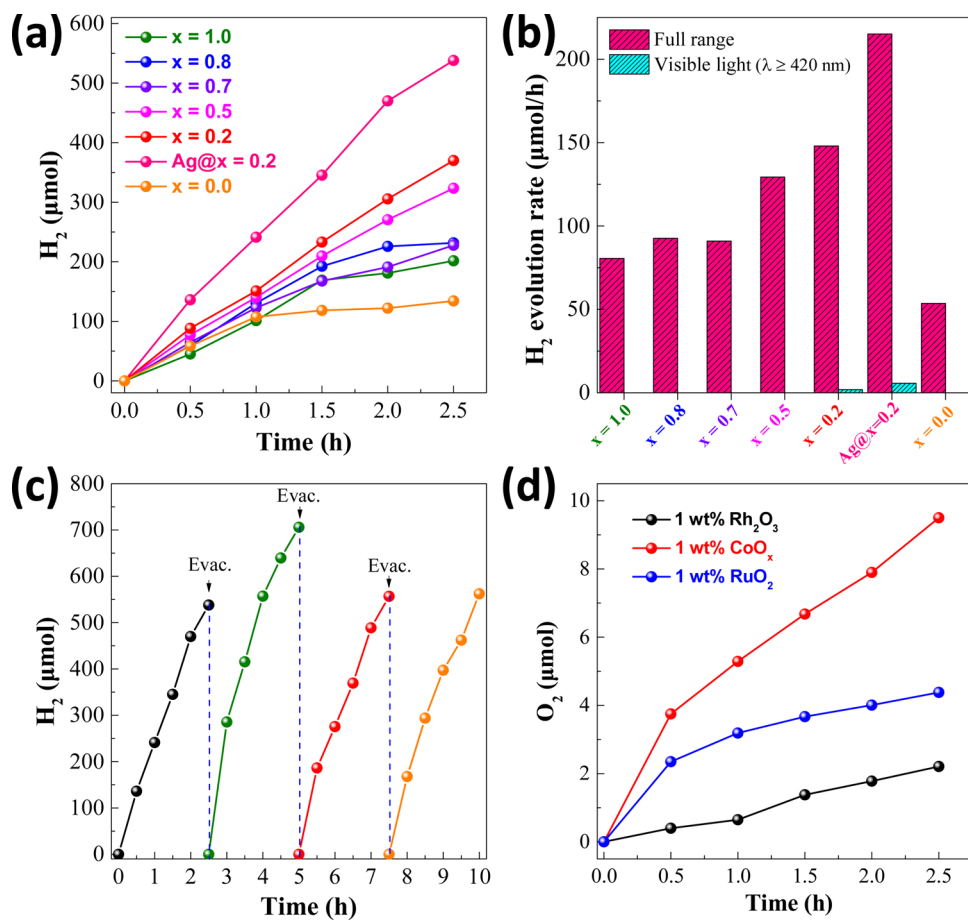


Fig. 7. (a) temporal photocatalytic hydrogen evolution of solid solutions $(\text{AgTaO}_3)_{1-x}(\text{SrTiO}_3)_x$ ($0.0 \leq x \leq 1.0$) under full range illumination ($\lambda \geq 250$ nm), $(\text{AgTaO}_3)_{0.8}(\text{SrTiO}_3)_{0.2}$ ($x = 0.2$) after reduction reactions was also included for comparisons; (b) average photocatalytic hydrogen evolution rate of all solid solutions under full range ($\lambda \geq 250$ nm) and visible light ($\lambda \geq 400$ nm) illumination; (c) repeated cycles of photocatalytic hydrogen evolution of sample $\text{Ag}@x = 0.2$, evacuation was performed at end of each cycle; (d) temporal photocatalytic oxygen evolution of sample $(\text{AgTaO}_3)_{0.8}(\text{SrTiO}_3)_{0.2}$ ($x = 0.2$) after reduction reactions under visible light illumination ($\lambda \geq 400$ nm), different cocatalysts such as 1 wt% Rh_2O_3 , 1 wt% CoO_x and 1 wt% RuO_2 were loaded onto sample powders for comparisons.

3.4. Photocatalytic hydrogen production

The photocatalytic activities of freshly prepared sample powders were evaluated by monitoring their hydrogen or oxygen evolution under full range ($\lambda \geq 250$ nm) or visible light ($\lambda \geq 400$ nm) illumination. Na_2SO_3 (0.05 M) or silver nitrate (0.05 M) aqueous solution were applied as sacrificial agent to promote photo-reduction or photo-oxidation reactions. The results are summarized in Fig. 7. All solid solutions demonstrated a much higher photocatalytic hydrogen activity than their parent compounds AgTaO_3 and SrTiO_3 under full range ($\lambda \geq 250$ nm) illumination. An optimal activity was found for sample $(\text{AgTaO}_3)_{0.8}(\text{SrTiO}_3)_{0.2}$ ($x = 0.2$) although it has the smallest surface area among all sample powders (Table 1). Its photocatalytic activity was further improved by exsolving Ag nanoparticles ($\text{Ag}@x = 0.2$) at the surface whereby hydrogen evolution is increased by nearly 45%. More interestingly, visible light photocatalytic hydrogen evolution was also achieved for $(\text{AgTaO}_3)_{0.8}(\text{SrTiO}_3)_{0.2}$ ($x = 0.2$) and exsolving Ag nanoparticles has clear enhancements to the performance. The average photocatalytic hydrogen production rate under both full range ($\lambda \geq 250$ nm) and visible light ($\lambda \geq 400$ nm) illumination are plotted in Fig. 7b. It is clear from Fig. 7b that $\text{Ag}@x = 0.2$ gives the highest hydrogen production rate $\sim 215.2 \mu\text{mol/h}$ for full range ($\lambda \geq 250$ nm) and $\sim 5.8 \mu\text{mol/h}$ for visible light ($\lambda \geq 400$ nm) illumination, corresponding to apparent quantum efficiency (AQE) $\sim 2.02\%$ and $\sim 0.11\%$, respectively. The photocatalytic activity was further examined by varying the amounts of Pt cocatalyst loaded and an optimal loading point was found to be 1 wt% (Figure S2). This experiment was also extended to additional cycles to evaluate its long term stability. As can be seen from Fig. 7c, the hydrogen production of sample $\text{Ag}@x = 0.2$ was maintained for four cycles in which $\sim 2363 \mu\text{mol}$ hydrogen was produced. Considering the amounts of catalyst used during the whole experiment

($\sim 326.6 \mu\text{mol}$), $\text{Ag}@x = 0.2$ is indeed an efficient photocatalyst. The photocatalytic activity of $\text{Ag}@x = 0.2$ is better than or at least comparable to similar photocatalytic systems containing plasmonic metal nanoparticles [36,47–50]. In addition, XRD analysis on sample $\text{Ag}@x = 0.2$ before and after photocatalytic experiment suggest no structure change (Figure S3), therefore $\text{Ag}@x = 0.2$ is a stable under current experiment conditions. More importantly, $\text{Ag}@x = 0.2$ is also active for photocatalytic oxygen production under visible light illumination ($\lambda \geq 400$ nm) if appropriate cocatalyst is loaded (Fig. 7d). Thereby, starting from two wide band gap semiconductors, we have successfully achieved visible light photocatalytic activity for both water reduction and oxygen reactions through the formation of solid solutions and exsolution of Ag nanoparticles.

3.5. Photoelectrochemical measurements

Photoelectrochemical (PEC) analysis was performed to elucidate the origin of the improved photocatalytic activities for solid solutions. Firstly, linear sweep voltammetry (LSV) under chopped light illumination was carried out on $(\text{AgTaO}_3)_{0.8}(\text{SrTiO}_3)_{0.2}$ ($x = 0.2$) and its parent compounds AgTaO_3 and SrTiO_3 . All samples reveal anodic photocurrent (Fig. 8a), indicative of n-type semiconductivity. The photocurrent of $(\text{AgTaO}_3)_{0.8}(\text{SrTiO}_3)_{0.2}$ ($x = 0.2$) is much higher than AgTaO_3 and SrTiO_3 under full range illumination ($\lambda \geq 300$ nm), being consistent with photocatalytic experiment. This phenomenon is also extended to visible light illumination ($\lambda \geq 400$ nm) in which anodic photocurrent is detected for $(\text{AgTaO}_3)_{0.8}(\text{SrTiO}_3)_{0.2}$ ($x = 0.2$) (Fig. 8b). This is in great contrast to AgTaO_3 and SrTiO_3 which show negligible photocurrent, verifying their wide band gap nature. Therefore, the better photocatalytic performance for solid solutions is at least in part due to their stronger light absorption. Secondly, open-circuit voltage

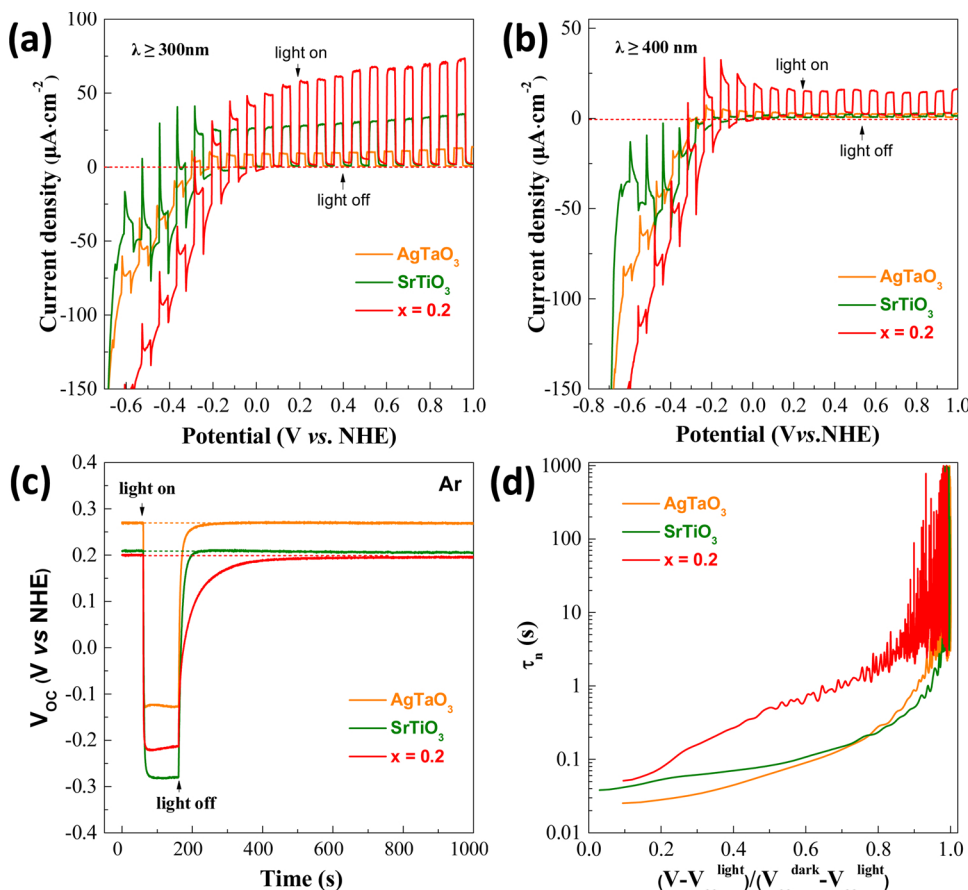


Fig. 8. (a) linear sweep voltammetry (LSV) for sample AgTaO₃ (x = 0.0), SrTiO₃ (x = 1.0) and (AgTaO₃)_{0.8}(SrTiO₃)_{0.2} (x = 0.2) under chopped full range illumination (λ ≥ 300 nm); (b) LSV for sample AgTaO₃ (x = 0.0), SrTiO₃ (x = 1.0) and (AgTaO₃)_{0.8}(SrTiO₃)_{0.2} (x = 0.2) under chopped visible light illumination (λ ≥ 400 nm); (c) open-circuit voltage decay curves for sample AgTaO₃ (x = 0.0), SrTiO₃ (x = 1.0) and (AgTaO₃)_{0.8}(SrTiO₃)_{0.2} (x = 0.2) under full range illumination (λ ≥ 300 nm), illumination was initiated when open-circuit voltage (V_{oc}) was stabilized in the dark and was terminated after 100 s; (d) the electron lifetime (τ_n) derived according to Eq. 2 as a function of normalized V_{oc}.

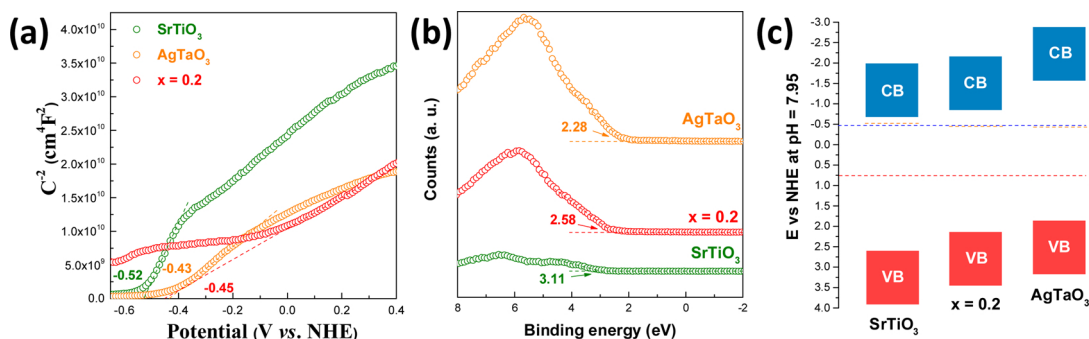


Fig. 9. (a) Mott-Schottky plots of sample AgTaO₃ (x = 0.0), SrTiO₃ (x = 1.0) and (AgTaO₃)_{0.8}(SrTiO₃)_{0.2} (x = 0.2), capacitance was extracted from impedance analysis at fixed frequency of 1000 Hz with 10 mV amplitude; (b) XPS valence band scan of sample AgTaO₃ (x = 0.0), SrTiO₃ (x = 1.0) and (AgTaO₃)_{0.8}(SrTiO₃)_{0.2} (x = 0.2); (c) schematic illustration of band edge positions of sample AgTaO₃ (x = 0.0), SrTiO₃ (x = 1.0) and (AgTaO₃)_{0.8}(SrTiO₃)_{0.2} (x = 0.2).

decay (OCVD) measurements were adopted to evaluate charge dissociation and dissipation conditions inside sample powders. Fig. 8c illustrates their OCVD curves using full range illumination (λ ≥ 300 nm). The negative shift of their open-circuit voltage (V_{oc}) in response to light illumination suggests accumulation of electrons in these sample powders, confirming again their n-type semiconductivity. However, upon terminating the light beam, both AgTaO₃ and SrTiO₃ reveal a rapid restoration of V_{oc} back to their original value in the dark, indicating fast charge dissipation phenomenon. As all these experiments were carried out in Ar atmosphere, a likely dissipation pathway is charge recombination between accumulation electrons and trapped holes. On the contrary, much longer OCVD curve is found for (AgTaO₃)_{0.8}(SrTiO₃)_{0.2} (x = 0.2) as it takes more than 500 s for a complete restoration of its V_{oc}. The lifetime of accumulated electrons can be quantitatively evaluated using the following equation [51,52]:

$$\tau_n = \frac{k_B T}{e} \left(\frac{dV_{oc}}{dt} \right)^{-1} \quad (2)$$

where τ_n is potential dependent lifetime, k_B is Boltzmann's constant, T is the temperature in K and e is the elementary charge. The function of τ_n with respect to normalized open-circuit voltage applied is plotted in Fig. 8d. Apparently, electrons in (AgTaO₃)_{0.8}(SrTiO₃)_{0.2} (x = 0.2) have nearly one order of magnitude longer lifetime than in AgTaO₃ and SrTiO₃. Thereby, charge separation conditions are significantly improved after the formation of solid solutions between AgTaO₃ and SrTiO₃.

To gain a deeper insight into the photocatalytic processes for solid solutions, band edge positions of (AgTaO₃)_{0.8}(SrTiO₃)_{0.2} (x = 0.2), AgTaO₃ and SrTiO₃ are determined. This is realized by combining Mott-Schottky (MS) analysis, XPS valence band scan and band gap values from UV-vis absorption spectra. MS analysis of these samples is

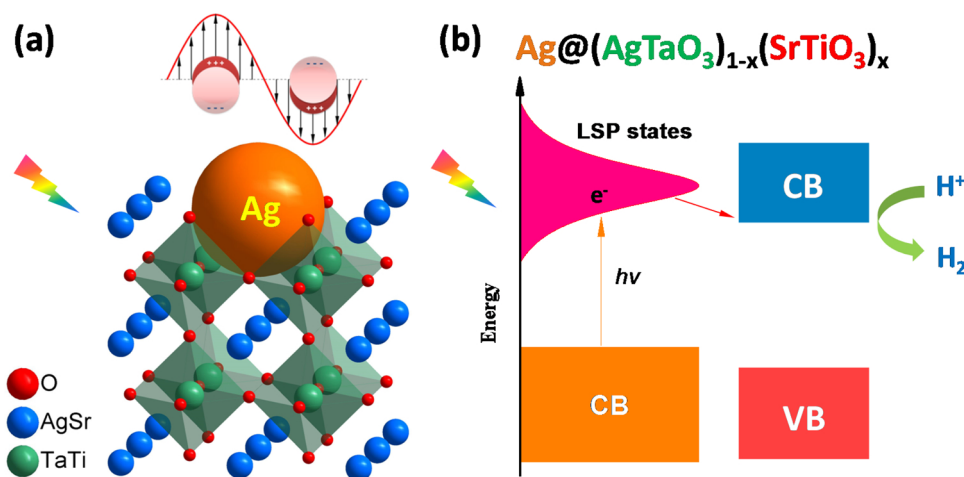


Fig. 10. (a) schematic illustration of Ag exsolution from solid solution $(\text{AgTaO}_3)_{1-x}(\text{SrTiO}_3)_x$ that has localized surface plasmons; (b) schematic representation of mechanism for water splitting on $\text{Ag}@x=0.2$.

illustrated in Fig. 9a. Their flat band positions, i.e. Fermi levels are deduced from extrapolating the linear part of MS curves down to potential axis, which are read to be -0.45 V , -0.43 V and -0.52 V vs NHE for $(\text{AgTaO}_3)_{0.8}(\text{SrTiO}_3)_{0.2}$ ($x = 0.2$), AgTaO_3 and SrTiO_3 , respectively. On the other hand, XPS valence band scan informs the relative energy gap between the top of valence band and their Fermi levels (Fig. 9b). Therefore, valence band edge positions can be deduced on the basis of above information. The conduction band edge positions can then be inferred by considering their band gap values. A schematic plot of all band edge positions for solid solutions ($x = 0.2$), AgTaO_3 and SrTiO_3 are illustrated in Fig. 9c. The band edge positions for AgTaO_3 and SrTiO_3 lie either too close or too far away from the redox potential of water, being inappropriate for solar water splitting reactions. Nevertheless, band edge positions for $(\text{AgTaO}_3)_{0.8}(\text{SrTiO}_3)_{0.2}$ ($x = 0.2$) settles approximately in the middle between AgTaO_3 and SrTiO_3 with substantially less separations, therefore, are quite suitable for solar water splitting reactions.

The mechanism for water splitting on $\text{Ag}@x = 0.2$ is then proposed and is illustrated in Fig. 10. Thermal treatment of $(\text{AgTaO}_3)_{1-x}(\text{SrTiO}_3)_x$ solid solutions in ethylene glycol results in exsolution of Ag nanoparticles at the surface which show localized surface plasmons in the visible light region. These Ag nanoparticles absorb visible light photons and inject hot electrons into $(\text{AgTaO}_3)_{1-x}(\text{SrTiO}_3)_x$ solid solutions that participate in water reduction reactions to produce hydrogen.

4. Conclusions

We have successfully synthesized complete solid solutions between AgTaO_3 and SrTiO_3 , i.e. $(\text{AgTaO}_3)_{1-x}(\text{SrTiO}_3)_x$ ($0.0 \leq x \leq 1.0$) via standard polymerized-complex method. The wet synthetic method significantly lowers down calcination temperature and favors phase formation. All samples adopt a cubic perovskite structure similar to SrTiO_3 and high temperature phase of AgTaO_3 . Thereby, introducing SrTiO_3 helps to stabilize AgTaO_3 in its high temperature cubic phase. The particle size of solid solutions is closely related to the level of SrTiO_3 in the structure and has a maximal point at $x = 0.2$. Impregnation of solid solutions ($x = 0.2$) into hot ethylene glycol leads to exsolution of Ag nanoparticles but with its crystal structure maintained. The band gap of solid solutions is clearly narrowed with respect to their parent compounds AgTaO_3 and SrTiO_3 , contributing to apparent absorption in the visible light region. Sample $(\text{AgTaO}_3)_{0.8}(\text{SrTiO}_3)_{0.2}$ ($x = 0.2$) has the smallest band value among all solid solutions. The appearance of Ag nanoparticles at its surface further increases its visible light absorption which turns the color of sample powders from yellowish white to yellow. Clear improvements on the photocatalytic hydrogen production

were realized on all solid solutions compared to their parent compounds AgTaO_3 and SrTiO_3 . An optimal point at $(\text{AgTaO}_3)_{0.8}(\text{SrTiO}_3)_{0.2}$ ($x = 0.2$) was found to give the highest activity among all samples. Its activity was further enhanced by 45% after exsolution of Ag nanoparticles at particle surface. More interestingly, visible light photocatalytic hydrogen production was achieved on $(\text{AgTaO}_3)_{0.8}(\text{SrTiO}_3)_{0.2}$ ($x = 0.2$) whose activity was clearly boosted by exsolution of Ag nanoparticles. Apparent quantum efficiency (AQE) $\sim 2.02\%$ and $\sim 0.11\%$ was recorded for $\text{Ag}@x = 0.2$ under full range and visible light illumination, and its photocatalytic activities were quite stable. In addition, photocatalytic oxygen production under visible light illumination was also noticed for sample $\text{Ag}@x = 0.2$ if proper cocatalyst was loaded. PEC analysis suggests the improved photocatalytic activity by forming solid solutions stems from an enhanced light absorption as well as better charge separation conditions. Besides, solid solutions ($x = 0.2$) own band edge positions that lie approximately in the middle between AgTaO_3 and SrTiO_3 with less energy separations, therefore, are appropriate for solar water splitting reactions.

Acknowledgements

We thank the National Natural Science Foundation of China (Grant No. 21401142, 51825204), Natural Science Foundation of Shanghai (Grant No. 19ZR1459200) for funding and Recruitment Program of Global Youth Experts (1000 plan). The work was also supported by Shanghai Science and Technology Commission (14DZ2261100), the Fundamental Research Funds for the Central Universities and the Laboratory of Precision Manufacturing Technology, China Academy of Engineering Physics (Grant No. ZD17006 < / GN3 > , < GN4 > ZZ16002).

Appendix A. Supplementary data

Supplementary material related to this article can be found, in the online version, at doi:<https://doi.org/10.1016/j.apcatb.2019.117818>.

References

- [1] N.S. Lewis, D.G. Nocera, Proc. Natl. Acad. Sci. U. S. A. 103 (2006) 15729–15735.
- [2] K. Maeda, K. Teramura, D.L. Lu, T. Takata, N. Saito, Y. Inoue, K. Domen, Nature 440 (2006) 295–295.
- [3] Z.G. Zou, J.H. Ye, K. Sayama, H. Arakawa, Nature 414 (2001) 625–627.
- [4] X.X. Xu, C. Randorn, P. Efstathiou, J.T.S. Irvine, Nat. Mater. 11 (2012) 595–598.
- [5] A. Kudo, Y. Miseki, Chem. Soc. Rev. 38 (2009) 253–278.
- [6] Z.B. Chen, T.F. Jaramillo, T.G. Deutsch, A. Kleiman-Shwarsstein, A.J. Forman, N. Gaillard, R. Garland, K. Takanabe, C. Heske, M. Sunkara, E.W. McFarland, K. Domen, E.L. Miller, J.A. Turner, H.N. Dinh, J. Mater. Res. 25 (2010) 3–16.

- [7] P. Reunchan, S.X. Ouyang, N. Umezawa, H. Xu, Y.J. Zhang, J.H. Ye, J. Mater. Chem. A 1 (2013) 4221–4227.
- [8] T. Ishii, H. Kato, A. Kudo, J. Photochem. Photobiol. A 163 (2004) 181–186.
- [9] W. Chen, H. Liu, X.Y. Li, S. Liu, L. Gao, L.Q. Mao, Z.Y. Fan, W.F. Shangguan, W.J. Fang, Y.S. Liu, Appl. Catal. B-Environ. 192 (2016) 145–151.
- [10] R. Asai, H. Nemoto, Q. Jia, K. Saito, A. Iwase, A. Kudo, Chem. Commun. 50 (2014) 2543–2546.
- [11] B. Modak, S.K. Ghosh, J. Phys. Chem. C 119 (2015) 7215–7224.
- [12] M. Miyauchi, M. Takashio, H. Tobimatsu, Langmuir 20 (2004) 232–236.
- [13] S.W. Bae, P.H. Borse, J.S. Lee, Appl. Phys. Lett. 92 (2008).
- [14] Y.A. Shevchuk, V.V. Gagulin, S.K. Korchagina, V.V. Ivanova, Inorg. Mater. 36 (2000) 739–741.
- [15] L.W. Lu, M.L. Lv, D. Wang, G. Liu, X.X. Xu, Appl. Catal. B-Environ. 200 (2017) 412–419.
- [16] L.W. Lu, M.L. Lv, G. Liu, X.X. Xu, Appl. Surf. Sci. 391 (2017) 535–541.
- [17] X.X. Xu, M.L. Lv, X.Q. Sun, G. Liu, J. Mater. Sci. 51 (2016) 6464–6473.
- [18] W.Y. Choi, A. Termin, M.R. Hoffmann, J. Phys. Chem. 98 (1994) 13669–13679.
- [19] H. Irie, Y. Watanabe, K. Hashimoto, J. Phys. Chem. B 107 (2003) 5483–5486.
- [20] M. Jansen, H.P. Letschert, Nature 404 (2000) 980–982.
- [21] G.Q. Zhang, S.R. Sun, W.S. Jiang, X. Miao, Z. Zhao, X.Y. Zhang, D. Qu, D.Y. Zhang, D.B. Li, Z.C. Sun, Adv. Energy Mater. 7 (2017).
- [22] J.S. Jang, P.H. Borse, J.S. Lee, S.H. Choi, H.G. Kim, J. Chem. Phys. 128 (2008).
- [23] D.K. Sharma, S. Hirata, L. Bujak, V. Bijju, T. Kameyama, M. Kishi, T. Torimoto, M. Vacha, Phys. Chem. Chem. Phys. 19 (2017) 3963–3969.
- [24] X.X. Xu, Y.H. Xie, S. Ni, A.K. Azad, T.C. Cao, J. Solid State Chem. 230 (2015) 95–101.
- [25] K. Iwashina, A. Kudo, J. Am. Chem. Soc. 133 (2011) 13272–13275.
- [26] H. Kato, K. Asakura, A. Kudo, J. Am. Chem. Soc. 125 (2003) 3082–3089.
- [27] S.X. Ouyang, H. Tong, N. Umezawa, J.Y. Cao, P. Li, Y.P. Bi, Y.J. Zhang, J.H. Ye, J. Am. Chem. Soc. 134 (2012) 1974–1977.
- [28] R.H. Mitchell, Perovskites: Modern and Ancient, Almaz Press Inc., Ontario, Canada, 2002.
- [29] W.J. Luo, Z.S. Li, X.J. Jiang, T. Yu, L.F. Liu, X.Y. Chen, J.H. Ye, Z.G. Zou, Phys. Chem. Chem. Phys. 10 (2008) 6717–6723.
- [30] M.L. Lv, Y.H. Xie, Y.W. Wang, X.Q. Sun, F.F. Wu, H.M. Chen, S.W. Wang, C. Shen, Z.F. Chen, S. Ni, G. Liu, X.X. Xu, Phys. Chem. Chem. Phys. 17 (2015) 26320–26329.
- [31] X.Q. Sun, G. Liu, X.X. Xu, J. Mater. Chem. A 6 (2018) 10947–10957.
- [32] X.Q. Sun, Y.L. Mi, F. Jiao, X.X. Xu, ACS Catal. 8 (2018) 3209–3221.
- [33] S.H. Wei, G. Zhang, X.X. Xu, Appl. Catal. B-Environ. 237 (2018) 373–381.
- [34] F.T. Wagner, G.A. Somorjai, Nature 285 (1980) 559–560.
- [35] H. Kato, H. Kobayashi, A. Kudo, J. Phys. Chem. B 106 (2002) 12441–12447.
- [36] X.X. Xu, G. Liu, A.K. Azad, Int. J. Hydrogen Energy 40 (2015) 3672–3678.
- [37] A.C. Larson, R.B. Von Dreele, Los Alamos National Laboratory Report No. LA-UR-86-748, (1994).
- [38] P. Van der Heide, X-ray Photoelectron Spectroscopy - An Introduction to Principles and Practices, John Wiley & Sons, Inc, Hoboken, New Jersey, 2012.
- [39] E.B. Hua, S. Jin, X.R. Wang, S. Ni, G. Liu, X.X. Xu, Appl. Catal. B-Environ. 245 (2019) 733–742.
- [40] E.B. Hua, G. Liu, G. Zhang, X.X. Xu, Dalton Trans. 47 (2018) 4360–4367.
- [41] Y.W. Wang, S. Jin, G.X. Pan, Z.X. Li, L. Chen, G. Liu, X.X. Xu, J. Mater. Chem. A 7 (2019) 5702–5711.
- [42] M. Valant, A.K. Axelsson, N. Alford, J. Eur. Ceram. Soc. 27 (2007) 2549–2560.
- [43] M. Valant, A.K. Axelsson, B. Zou, N. Alford, J. Mater. Res. 22 (2007) 1650–1655.
- [44] U. Farid, H.U. Khan, M. Avdeev, S. Injac, B.J. Kennedy, J. Solid State Chem. 258 (2018) 859–864.
- [45] R.D. Shannon, C.T. Prewitt, Acta Crystallogr. B 25 (1969) 925–946.
- [46] M.L. Lv, G. Liu, X.X. Xu, Acs Appl. Mater. Interfaces 8 (2016) 28700–28708.
- [47] D. Saadetejad, R. Yildirim, Int. J. Hydrogen Energy 43 (2018) 1116–1122.
- [48] M. Li, J.Y. Zhang, W.Q. Dang, S.K. Cushing, D. Guo, N.Q. Wu, P.G. Yin, Phys. Chem. Chem. Phys. 15 (2013) 16220–16226.
- [49] S.W. Cao, J. Fang, M.M. Shahjamali, F.Y.C. Boey, J. Barber, S.C.J. Loo, C. Xue, RSC Adv. 2 (2012) 5513–5515.
- [50] C.G. Silva, R. Juarez, T. Marino, R. Molinari, H. Garcia, J. Am. Chem. Soc. 133 (2011) 595–602.
- [51] A. Zaban, M. Greenshtein, J. Bisquert, ChemPhysChem 4 (2003) 859–864.
- [52] B.H. Meekins, P.V. Kamat, ACS Nano 3 (2009) 3437–3446.